Analysis of drift-gradient instabilities and associated transport in a magnetic nozzle plasma

M. Ripoli,* E. Ahedo† and M. Merino‡

Department of Aerospace Engineering,
Universidad Carlos III de Madrid, Leganés, 28911, Spain

Abstract

$E \times B$ partially-magnetized discharges such as in electrodeless plasma thrusters are susceptible to instability-driven anomalous cross-field transport. The first part of this work presents a linear analysis for fluid electrostatic waves in two-dimensionally inhomogeneous $E \times B$ plasmas, introducing the effect of inhomogeneities along the magnetic field on the destabilization of the medium. The unstable modes in the absence of collisions are found to be a generalization of the lower-hybrid drift instability (LHDI). The dispersion relation is then applied to the simulation data of a magnetic nozzle plume at equilibrium, revealing the importance of including parallel gradients in the formulation. Quasi-linear analysis is performed to model the second-order cross-field electron flux. This is found to be directed against the zeroth-order gradients, therefore reducing the energy source for the instabilities. In the last part of this work a discussion on the preliminary methodology and mathematical model to perform global kinetic non-linear simulations of cylindrical plasmas is presented, employing a Particle-in-Cell scheme in the r-z plane and a spectral Particle-in-Fourier method in the azimuthal direction.

1 Introduction

Several plasma devices, and in particular many space plasma thrusters, operate as partially magnetized $E \times B$ discharges, with electrons closely following magnetic field lines and ions moving almost freely from magnetic forces effects. Two notable examples are Hall Thrusters [1, 2, 3] and Electrodeless Plasma Thrusters (EPTs)[4, 5, 6, 7, 8, 9, 10]. The latter rely on a magnetic nozzle (MN) [11, 12, 13] as their accelerating stage, which consists of a converging-diverging magnetic field that confines the lateral plasma expansion, transforming thermal energy into directed kinetic energy, resulting in a high-velocity plasma jet. $E \times B$ plasmas, like the one in a MN, are known to be subject to oscillations, instabilities, and turbulence [14], which under certain circumstances, can lead to non-classical transport of electrons across magnetic field lines, suggesting the existence of additional mechanisms not captured by usual steady-state electron models.

Recent experimental works reveal the presence of both azimuthal oscillations extending up to the hundreds of kHz [15, 16, 17] and azimuthal-axial oscillations up to a few MHz [18, 19]. Whether the instability-driven electron flux is outward or inward remains a topic of discussion [18, 15].

In presence of non-zero inter-species drifts, instabilities may arise. When these drifts are caused by the existence of gradients at right angles with the background magnetic field, the resulting instabilities can be either collisionless *drift-gradient instabilities* or collisional *drift-resistive instabilities*.

The most notable example of drift-gradient instability are the lower-hybrid drift instability (LHDI) [20, 21, 22] and its simplified zero-electron Larmor radius limit version [23], known as the modified

*Ph.D. student, mripoli@ing.uc3m.es
†Full professor, eahedo@ing.uc3m.es
‡Full professor, mario.merino@uc3m.es

Copyright 2025 by the Electric Rocket Propulsion Society. All rights reserved.

collisionless variant of the Simon-Hoh instability [24]. If wave propagation parallel to $\boldsymbol{B}$ is to be considered, an instability to consider is the modified two-stream instability (MTSI) [25, 26, 27, 28].

Most of the studies of the LHDI rely on a description of plasmas presenting inhomogeneities only in the direction *perpendicular* to $\boldsymbol{B}$ and analyze only modes with perpendicular propagation. While this might be satisfactory for devices such as a Hall thruster, where most magnetic lines connect two adjacent walls, it is expected to be insufficient for MNs, where magnetic lines extend very far. In addition, a suitable model for fluctuations in a MN must also take into account the 2D magnetic topology, including field curvature, and the dominant gyroviscous effects on electrons.

The study of time-resolved dynamics of an electrostatic plasma discharge requires solving the non-linear kinetic equation for each one of the plasma species and to couple them through Poisson's equation. This can be done numerically by means of the Particle-In-Cell (PIC) method, where charged macroparticles are moved independently under the action of the background magnetic field and the time-varying electric potential. This scheme has been widely used in studying both HT [29, 30] and MN plasmas [31, 32], and in simulating the evolution and non-linear effects of fluctuations in $E \times B$ discharges [33]. Most PIC schemes compute the fields through finite differencing (FD) on a grid and then interpolate them on the particle position. This leads to the well-known finite-grid instability [34] and to spurious heating, violating the energy balance. Given the large computational times that come with this method, most of the analyses are usually limited to a 2D space in physical coordinates and to a 3D phase space. Their restriction to two dimensions requires the introduction of semi-empirical parameters to account for the effect of the plasma dynamics in the missing dimension, such as *ad hoc* anomalous collision coefficients in axial-radial simulations to account for turbulence in the azimuthal direction [35]. The inclusion of azimuthal dynamics of particles is essential for the self-consistent characterization of wave-driven plasma transport.

As an alternative to FD, macroscopic fields can be expanded as Fourier series and can be applied on the particle position without the need of interpolating. Particle-In-Fourier (PIF) schemes do precisely this, containing the numerical imprecisions due to discretization and interpolation and effectively eliminating the nonphysical effects due to the finiteness of the grid. These methods allow for the conservation of both momentum and energy [36]; as a drawback they impose an upper bound on the number of spatial modes that can be resolved, filtering out higher modes in the plasma power spectrum. To obtain a similar spectral resolution as that given by finite differencing, one would have to include as many modes as the number of grids that a FD method would require [34].

In the first part of this work we derive a complete linear dispersion relation for local electrostatic drift waves, including 2D gradients and 3D wave propagation, keeping inertial, gyroviscous, and collisional effects in our formulation. This derivation, carried out from a fluid framework, assuming cold, unmagnetized ions and warm electrons, focuses on frequencies much smaller than the electron cyclotron one, on wavelengths larger than the electron Larmor radius, and on electron drifts much smaller than the electron thermal velocity. The inclusion of parallel gradients is found to substantially widen the parametric region associated to instabilities. The obtained dispersion relation is then applied to equilibrium data in a MN, found using hybrid PIC/fluid/wave simulations by Jimenez et al. [37], as input for the equilibrium plasma quantities and gradients. The findings are qualitatively contrasted with available experimental data. Lastly, quasi-linear theory is applied to determine the second-order instability-driven electron currents.

A preliminary version of this formulation has been presented previously as a conference paper [38], where an iterative procedure to consistently derive the dispersion relation in the case $u_{e0} = O(c_{e0})$, not covered in the present work, was discussed as well. This work has been recently published in [39].

In the second part, we present preliminary methodology and mathematical model for a mixed PIC/PIF architecture to study $E \times B$ discharges, highlighting the potential advantages that this approach may bring, over performing full 3D simulations, when the number of relevant azimuthal modes is small (likely, up to tens or hundreds of modes).

The rest of the paper is structured as follows: in section 2 we provide our fluid framework, from which the general dispersion relation is derived. Said relation is presented in 2.2, and its main unstable modes are commented as well. A link to a computational notebook file including the detailed derivation

Copyright 2025 by the Electric Rocket Propulsion Society. All rights reserved.

of several key parts of the dispersion relation is provided at the end of the paper, in the Data Availability section. In section 3 we apply the linear model to the data from Jimenez et al. [37] to discuss the expected instabilities in an illustrative MN case. In section 4 we discuss the effect of the resulting oscillations on cross-field fluxes and velocities through a quasi-linear analysis. In section 5, the mathematical model behind the PIC/PIF architecture is presented, and its main advantages and challenges discussed. This last part of the manuscript represents a work-in-progress, and no quantitative results are available yet. Finally, section 6 summarizes the main findings of this work.

2 Fluid model for local linear electrostatic waves

We consider a two-fluid plasma composed of cold, unmagnetized ions i, and warm, magnetized electrons e, under the action of an applied magnetic field $\boldsymbol{B}$. Two orthonormal frames of reference are used: a Cartesian one $\{\mathbf{1}_z, \mathbf{1}_r, \mathbf{1}_\theta\}$, with coordinates (z, r, θ); and a magnetic one $\{\mathbf{1}_\parallel, \mathbf{1}_\perp, \mathbf{1}_\theta\}$with $\mathbf{1}_\parallel = \boldsymbol{B}/B$. The plasma response is constituted by an equilibrium (steady-state) solution independent of θ, and a small-amplitude perturbation. Thus, any plasma quantity, say Q, is expressed as

$$Q(\boldsymbol{x},t) = Q_0(\boldsymbol{x}) + \frac{1}{2}[Q_1(\boldsymbol{x})\exp(i\boldsymbol{k}\cdot\boldsymbol{x} - i\omega t) + CC], \tag{1}$$

with Q_0 and Q_1 the equilibrium and perturbation parts, respectively; $\boldsymbol{x} = s_\perp \mathbf{1}_\perp + s_\theta \mathbf{1}_\theta + s_\parallel \mathbf{1}_\parallel$, being $s_\perp$, s_θ, $s_\parallel$ local coordinates at the point under analysis; $\boldsymbol{k}$ real wavevectors and $\omega = \omega_r + i\gamma$ complex frequencies; and CC means complex conjugate. We will look for eigenmodes of the perturbation problem with $\gamma > 0$, i.e., we seek the local, linear instabilities of the problem.

We derive the perturbation equations for a generic equilibrium response, taking into consideration perpendicular and parallel gradients on the equilibrium magnitudes, plus collisional effects on the electrons. To account properly for FLR effects on electrons, the fluid formulation of the gyroviscous tensor is included in the model. We focus on the frequency range $\omega \leq O(\omega_{LH}) \ll \omega_{ce}$, with $\omega_{LH} = eB/\sqrt{m_e m_i}$ the lower-hybrid frequency and ω_{ce} the electron gyrofrequency. We will expand the perturbation equations in the small mass-ratio parameter $\varepsilon = \sqrt{m_e/m_i}$, and the expansion will assume that $\rho_e/L_j = O(\varepsilon)$, with ρ_e the electron gyroradius and L_j the gradient lengths of the different plasma magnitudes at equilibrium.

The perturbation model here disregards the fluctuations of the electron temperature T_e, an assumption that has been deemed reasonable for low-frequency oscillations [40]. The plasma is assumed weakly inhomogeneous, that is, for any generic plasma quantity Q, its second-order spatial derivatives $\nabla^2 \ln Q$ will be neglected to order ε. On the contrary, the gradients of the first-order quantities Q_1 in Eq. (1) are needed and they are composed of two contributions,

$$(\nabla Q)_1 = \frac{1}{2}\left[(i\boldsymbol{k}Q_1 + \nabla Q_1)\exp(i\boldsymbol{k}\cdot\boldsymbol{x} - i\omega t) + CC\right], \tag{2}$$

with $|\nabla \ln Q_1| k^{-1} = O(\varepsilon)$ by assumption. Finally, for brevity, we shall drop the subscript 0 on quantities that do not feature a first-order variation in our model, such as the magnetic field and electron temperature, i.e. $B \equiv B_0$, $T_e \equiv T_{e0}$.

2.1 General two-fluid equations

Warm, magnetized electrons are described by their continuity and momentum equations, which read:

$$\frac{\partial n_e}{\partial t} + \nabla\cdot(n_e \boldsymbol{u}_e) = \nu_p n_e, \tag{3}$$

$$\frac{\partial \boldsymbol{u}_e}{\partial t} + \boldsymbol{u}_e\cdot\nabla\boldsymbol{u}_e = -\frac{\nabla\cdot\overline{\overline{p}}_e}{m_e n_e} - \frac{e}{m_e}(-\nabla\phi + \boldsymbol{u}_e\times\boldsymbol{B}) - \nu_e \boldsymbol{u}_e, \tag{4}$$

where ν_p represents the particle production rate, ϕ the electrostatic potential, ν_e is used to model dissipative forces on the electrons coming from collisional phenomena, and $\overline{\overline{p}}_e$ the complete electron pressure

Copyright 2025 by the Electric Rocket Propulsion Society. All rights reserved.

tensor including the gyroviscous contribution. The system is closed without an energy equation, as we are neglecting temperature perturbations, i.e., $T_{e1} \equiv 0$.

Cold, unmagnetized, singly-charged ions are described by the same Eqs. (3) to (4), neglecting the magnetic force ($B = 0$), pressure tensor ($\overline{\overline{p}}_i = 0$), and collisional momentum exchange ($\nu_i = 0$).

The zeroth solution is allowed to feature perpendicular and parallel gradients of $\boldsymbol{B}$, n_0, and T_0, over a characteristic length L. The azimuthal electron velocity is constituted by an $E \times B$ drift and a diamagnetic drift, in the range

$$c_s \ll u_{\theta e} \ll c_e, \tag{5}$$

with $c_s = \sqrt{T_e/m_i}$ and $c_e = \sqrt{T_e/m_e}$ the ion-sound and the electron-thermal velocities, while the rest of the electron velocity components and the ion velocity are smaller:

$$u_{\perp e0}, u_{\parallel e0} \leq O(c_s), \qquad u_{i0} = O(c_s). \tag{6}$$

Doppler-shifted frequencies for electrons and ions in the perturbation problem are defined as

$$\omega_j \equiv \omega - \boldsymbol{k} \cdot \boldsymbol{u}_{j0}, \qquad j = e, i. \tag{7}$$

2.2 The dispersion relation and main instability modes

Ref. [39] addresses the derivation of the linear relation between the normalized density $h_{e1} = n_{e1}/n_0$ and ϕ_1, carrying out the linearization of Eqs. (3) and (4), and expanding in terms of the small parameter $\varepsilon = \rho_e/L$, considering $\omega_e/\omega_{ce} = O(\varepsilon)$. There are several customary frequencies involving zeroth-order magnitudes, their gradients, and $\boldsymbol{k}$, defined as

$$\Delta = \boldsymbol{k} \cdot (\boldsymbol{u}_{e0} - \boldsymbol{u}_{i0}) \equiv \omega_i - \omega_e \,, \qquad \omega_{E\times B} = k_\theta \frac{\nabla_\perp \phi_0}{B} \equiv \frac{k_\theta c_e^2}{\omega_{ce}} \frac{e\nabla_\perp \phi_0}{T_e} \,, \tag{8}$$

$$\omega_B = -\frac{k_\theta c_e^2}{\omega_{ce}} \nabla_\perp \ln B \qquad \omega_N = -\frac{k_\theta c_e^2}{\omega_{ce}} \nabla_\perp \ln n_0 \,, \qquad \omega_T = -\frac{k_\theta c_e^2}{\omega_{ce}} \nabla_\perp \ln T_e \,, \tag{9}$$

$$\omega_{M\perp} = -\frac{k_\theta c_e^2}{\omega_{ce}} \nabla_\perp \ln \frac{p_{e0}}{B^2} \equiv \omega_N + \omega_T - 2\omega_B \,, \qquad \omega_{M\parallel} = -\frac{k_\theta c_e^2}{\omega_{ce}} \nabla_\perp \ln \left(\frac{p_{e0}}{B^4}\right) \equiv \omega_N + \omega_T - 4\omega_B \,, \tag{10}$$

$$\omega_{M'} \equiv \omega_N - 2\omega_B - k^2\rho_e^2\omega_T/2, , \qquad \omega_\parallel = c_e \left(1 + \frac{k^2\rho_e^2}{2}\right) \sqrt{k_\parallel^2 + \frac{1}{4}\left[\nabla_\parallel \ln \frac{p_{e0}}{B} - \frac{k^2\rho_e^2}{1 + k^2\rho_e^2/2} \nabla_\parallel \ln B\right]^2} \,. \tag{11}$$

The frequency $\omega_\parallel$ contains the combined effects of wave parallel propagation and parallel gradients of 0th-order magnitudes. $\omega_{M\perp}$ and $\omega_{M\parallel}$ describe the Doppler shift in the inertial response of the electrons to variations of ϕ_1 and h_{e1}, the former in the perpendicular plane, the latter along the magnetic field, and are strictly related to the magnetization velocity of the electrons [41, 42].

The resulting dispersion relation is [39]

$$\frac{k^2 c_s^2}{\omega_i^2} = \frac{[\omega_{M'} + k^2\rho_e^2(\omega_e + i\nu_e)](\omega_{M\parallel} + \omega_e + i\nu_e) - \omega_\parallel^2}{(\omega_e + \omega_{M\perp} + ik^2\rho_e^2\nu_e)(\omega_e + \omega_{M\parallel} + i\nu_e)}, \tag{12}$$

whose solutions are electrostatic waves for an inhomogeneous plasma with parallel effects (both propagation and gradient ones) in the low-drift regime $\omega \leq \omega_{LH}$. This equation is a fourth-order polynomial on ω. For our plasma conditions (5) and (6), the frequency shift parameter Δ reduces to

$$\Delta \simeq k_\theta u_{\theta e0} = \omega_{E\times B} + \omega_N + \omega_T, \tag{13}$$

with $\omega_{E\times B}$ and $(\omega_N + \omega_T)$ the contributions of the $E \times B$ and the diamagnetic drifts, respectively. Observe then, that the combination $\omega_e + \omega_{M\perp} \simeq \omega - \omega_{E\times B} - 2\omega_B$ in the denominator of Eq. (12), implies the cancellation of the diamagnetic drift [42].

Copyright 2025 by the Electric Rocket Propulsion Society. All rights reserved.

To analyze the dispersion relation (12) we will focus on the ranges

$$k\rho_e \lesssim O(1), \quad \Delta \sim \omega_{LH} \sim \omega_{LH} - |\Delta|, \qquad \omega_B \sim \omega_N \sim \omega_T \leq O(\omega_{LH}), \quad \omega_{\parallel} \ll \omega_{LH}, \tag{14}$$

with $kc_s \ll |\Delta|$. First we will comment three collisionless case: the case without parallel effects, then the one without perpendicular gradients, and finally the general case. The effect of collisions will be discussed right after.

Neglecting all parallel effects we get the dispersion relation relevant for LHDI and SHI, and it is amply treated in the literature. Eq. (12) becomes a third-order polynomial on ω, whose solutions comprise an electron mode and two ion modes, which become lower-hybrid waves in the homogeneous case [42]. As shown in [39], the two lower-hybrid ion modes satisfy for $k^2\rho_e^2 \ll |\omega_{M'}|/\omega_{LH}$

$$\omega_i = \frac{k^2c_s^2}{\omega_{M'} - k^2\rho_e^2\Delta}\left(\frac{1}{2} \pm \sqrt{\frac{1}{4} - \frac{\omega_{M'} - k^2\rho_e^2\Delta}{k^2c_s^2}(\Delta - \omega_{M\perp})}\right). \tag{15}$$

One of these ion modes is unstable for

$$4(\omega_{M'} - k^2\rho_e^2\Delta)(\Delta - \omega_{M\perp}) > k^2c_s^2, \tag{16}$$

which is the criterion for the fluid LHDI derived by Krall and Liewer [20]. In the limit $k\rho_e \to 0$, a modification of the SHI criterion as in [23] is readily obtained.

Dropping perpendicular gradients and collisions, the dispersion relation and setting the derivative of (12) with respect to ω equal to 0 we get the following (exact) instability criterion

$$\left(\frac{\omega_{\parallel}}{kc_s}\right)^{2/3} > \left(\frac{|\Delta|}{\omega_{LH}}\right)^{2/3} - 1. \tag{17}$$

For $|\Delta| > \omega_{LH}$, this expression yields the range of $\omega_{\parallel}$ where the instability develops. For $|\Delta| < \omega_{LH}$, the instability is present for any $\omega_{\parallel}$. In the case of zero parallel gradients, $|\Delta|/\omega_{LH} \gg 1$, and $k\rho_e \to 0$, Eq. (17) reduces to

$$k_{\parallel}/k > |\Delta|/\omega_{LH}, \tag{18}$$

which is the usual MTSI criterion [43, 27]. Equation (17) can thus be considered a generalization of the MTSI criterion in two ways: one, into the range $|\Delta|/\omega_{LH} \leq O(1)$, second, on the contribution of parallel gradients.

The derivation of the frequencies of the ion modes from the 4th-order polynomial is cumbersome and is reported in [39]. The result, valid for $k^2\rho_e^2 \ll |\omega_{M'}|/\omega_{LH}$ and $\omega_{\parallel} \gg kc_s$, is

$$\omega_i = \frac{k^2c_s^2}{2}\frac{\Delta - \omega_{M\parallel}}{(\omega_{M'} - k^2\rho_e^2\Delta)(\Delta - \omega_{M\parallel}) + \omega_{\parallel}^2}\left\{1 \pm \sqrt{1 - 4\frac{\Delta - \omega_{M\perp}}{\Delta - \omega_{M\parallel}}\frac{(\omega_{M'} - k^2\rho_e^2\Delta)(\Delta - \omega_{M\parallel}) + \omega_{\parallel}^2}{k^2c_s^2}}\right\}. \tag{19}$$

Therefore, one ion mode is unstable for

$$4(\omega_{M'} - k^2\rho_e^2\Delta)(\Delta - \omega_{M\perp}) > k^2c_s^2 - 4\omega_{\parallel}^2\frac{\Delta - \omega_{M\perp}}{\Delta - \omega_{M\parallel}}. \tag{20}$$

This condition is a generalization of the LHDI criterion (16), in the presence of parallel effects. For

$$-1 < \omega_B/\omega_{E\times B} < -1/2, \tag{21}$$

parallel effects reduce the instability range.

Copyright 2025 by the Electric Rocket Propulsion Society. All rights reserved.

2.2.1 Collisional effects

If collisions are taken into account in the dispersion relation (i.e. $\nu_e > 0$) resistive and drift-resistive unstable modes appear. The case with perpendicular gradients and no parallel effects has been treated amply in the literature. Ramos et al. [42] have made a detailed discussion finding that collisions widen the parametric region of instability. This is also true for $\omega_{\parallel} = 0$. and lower the peak growth rate of drift-gradient instabilities predicted in the collisionless case.

When the plasma is destabilized by collisionless effects, collisions lower the growth rate for $\omega_{\parallel} = 0$: when parallel effects are included, collisions have a positive contribution to the growth rate for

$$\frac{\omega_{M'} - k^2\rho_e^2\Delta}{\Delta - \omega_{M\parallel}} < -k^2\rho_e^2. \tag{22}$$

3 Drift-gradient instabilities in a magnetic nozzle

The development of drift-gradient instabilities in different points of the MN region of a helicon plasma thruster, presented in Ref. [37], is analyzed in this Section, by considering the dispersion relation (12).

The equilibrium solution in that model was obtained with a multiple-formulation (PIC/fluid/wave) code. The fluid electron model is drift-diffusive, with no FLR effects and an isotropic pressure. Electron collisions corresponded to different elastic and inelastic processes. Figure 1 plots maps of several plasma magnitudes in a subdomain of the whole MN region simulated in Ref. [37].

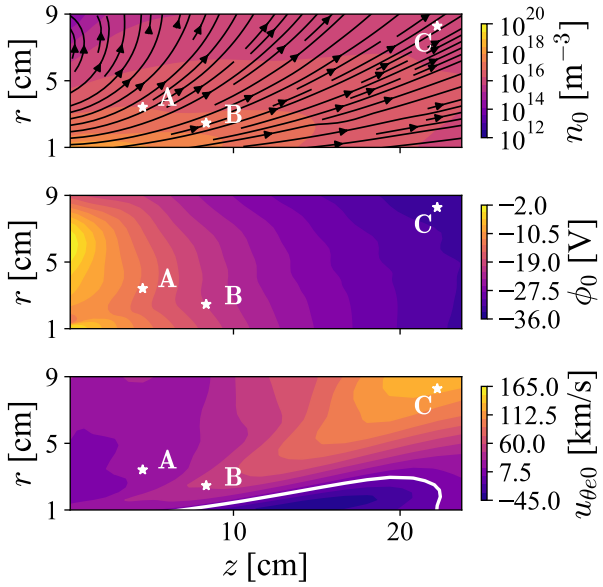

Figure 1: Contour plots for n_0, ϕ_0 and $u_{\theta e0}$, for the simulation data of the plasma expansion in the magnetic nozzle of a helicon plasma thrsuter, from Ref. [[37]]. White dots indicate the three points for which a dedicated ω_i-k analysis is presented in subsequent figures. In the plot of n_0, $\boldsymbol{B}$ streamlines have been superimposed. The white line represents the $u_{\theta e0} = 0$ line.

We now move on to the identification of the most unstable modes at each point of the MN domain of Fig. 1, as predicted by the dispersion relation (12). For each point of the map, the maximum growth rate $\gamma_{max} = \max(\gamma(\boldsymbol{k}))$, considering all branches, has been obtained, with the associated wavenumber and real frequency in the laboratory frame $\boldsymbol{k}^*$, ω_r^*, respecting the conditions$k^*\rho_e^* < 1$ and $|k_{\parallel}^* c_e| < |\omega_e^*|$. The mode associated with γ_{max} is then the most unstable one for that particular point of the MN; 2D maps of γ_{max}, ω_r^* and $\boldsymbol{k}^*$ are shown in Figure 2. The condition needed for our Cartesian expansion to be valid, i.e. $|rk_\theta| \gg 1$, has been relaxed to analyze the neighborhood of the axis.

Copyright 2025 by the Electric Rocket Propulsion Society. All rights reserved.

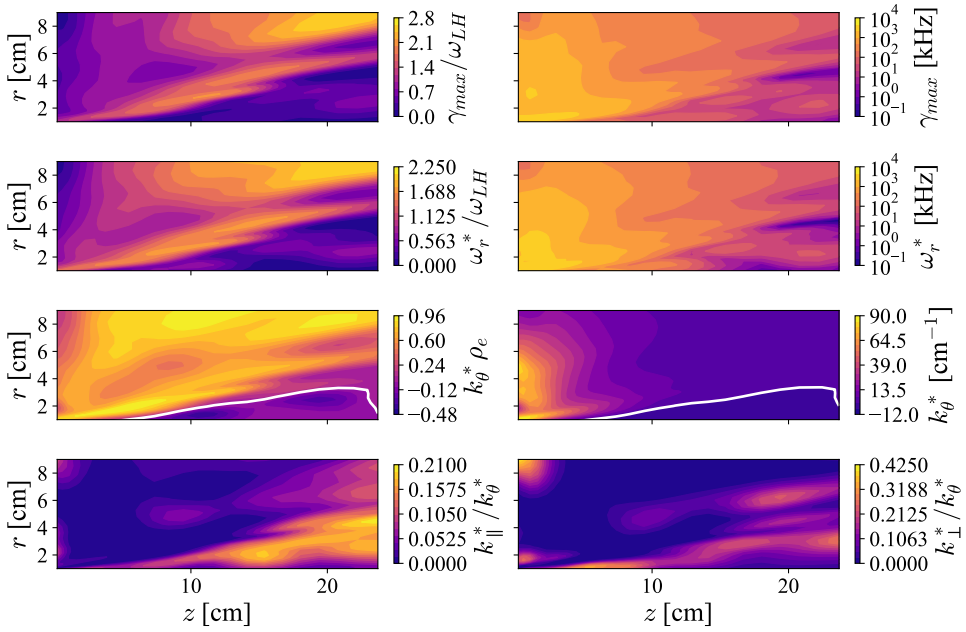

Figure 2: 2D maps of γ_{max}, ω_r^*, $\boldsymbol{k}_\theta^*$ and $k_\perp^*$ resulting from a point-wise local analysis across the MN plume region in the collisionless limit. The white line represents the $k_\theta^* = 0$ line.

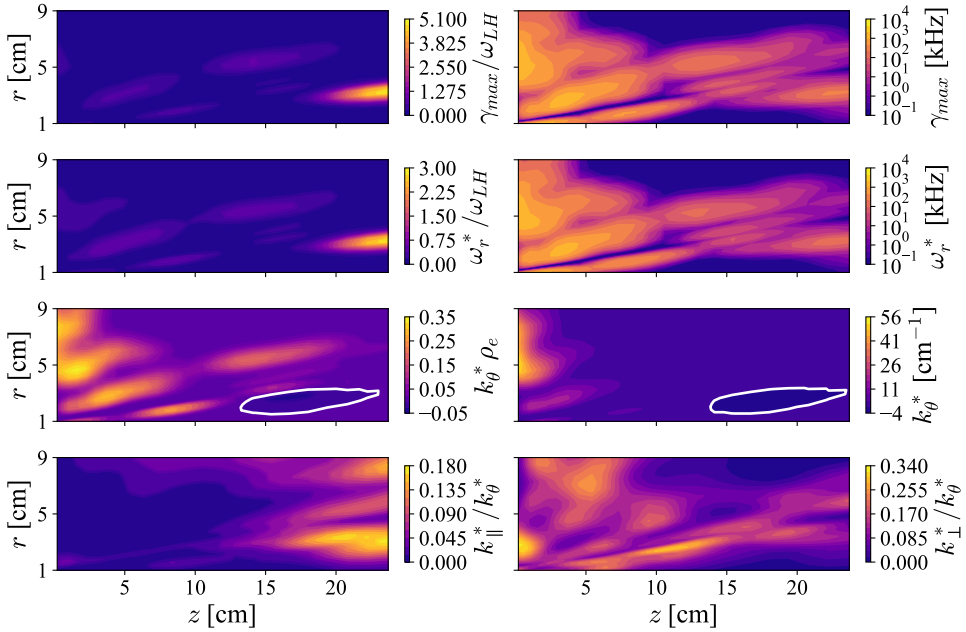

Figure 3: Similar to figure 2, but removing parallel gradient effects in the dispersion relation.

Copyright 2025 by the Electric Rocket Propulsion Society. All rights reserved.

Parallel gradients play a major role in the stability of the solution, allowing the onset of instabilities in those points of the MN where the classical LHDI criterion from Eq. (16) does not hold, even with $k_{\parallel} = 0$. The criterion for destabilization from parallel gradients is given in Eq. (20).

The effect of collisionless is negligible, as shown in [39].

A qualitative comparison with the available experimental data is needed, but limited by the fact that experimental data depicts the (non-linearly) *saturated* fluctuations. In Figure 2 we have shown that the most unstable modes predicted by our model consist of mainly-azimuthal waves with associated real oscillation frequency ω_r^* in the 1 kHz–1 MHz range. In [18] and [19] fluctuations are found in a similar frequency range in the MN of their respective devices, but waves exhibit a large $k_{\parallel}$, introducing important kinetic effects. In the works of [15] and [17], fluctuations are detected in the 10–100 kHz range and consist of mostly azimuthal waves, and are identified as magnetosonic waves in the former and acoustic waves non-linearly excited by the helicon pump wave in the latter. Our model offers that an alternative linear explanation to either of them, based on the presence of parallel gradients.

4 Quasi-linear cross-field transport

In the collisionless case, the electron cross-field current at the zeroth order is ideally null. To tackle the effect of linear perturbations on cross-field electron transport we quantify, through a limited quasi-linear analysis, when and how the fluctuations can nonlinearly produce a second-order contribution to the electron current field.

The second-order terms arising from the interaction of a single mode of complex frequency $\omega = \omega_r + i\gamma$ with itself are comprised of a quasi-DC axysimmetric part, varying in time with exponent $2\gamma t$, and a double-frequency oscillatory part. Since we want to gauge how instabilities affect the equilibrium over time, it is only the quasi-DC part that we are interested in. For this purpose, we extend the definition of our plasma quantities with respect to equation (1), their expression now being

$$Q(\boldsymbol{x},t) = Q_0(\boldsymbol{x}) + \frac{1}{2}[Q_1(\boldsymbol{x})\exp(i\boldsymbol{k}\cdot\boldsymbol{x} - i\omega t) + CC] + Q_2(\boldsymbol{x})\exp(2\gamma t) + \dots \tag{23}$$

This expansion is not uniformly valid for all times; the second-order term will eventually result in a modification of Q_0. We then restrict our analysis to the time interval for which this expansion is valid. The quasi-DC, real part of the product two generic first-order quantities, say a_1 and b_1, is

$$\langle a_1 b_1^* \rangle = \frac{a_1 b_1^* + a_1^* b_1}{4}\exp(2\gamma t). \tag{24}$$

For the cross-field transport, we are interested in the second order, quasi-DC, perpendicular electron flux, which, after normalizing with $\exp(2\gamma t)$, is given by:

$$(n_e u_{\perp e})_2 = n_0 \langle u_{\perp e1} h_{e1}^* \rangle \exp(-2\gamma t) + n_0 u_{\perp e2}\,. \tag{25}$$

The term $\langle u_{\perp e1} h_{e1}^* \rangle$ by taking the quasi-DC real part of the product between $u_{\perp e1}$ and h_{e1} from [39]. $u_{\perp e2}$ can be found as a function of $|\phi_1|^2$ from the second-order expression of the momentum conservation along θ. Their normalized contributions have been plotted in Figure 4 for the simulation data of Section 3. From the figure it can be seen that the second order cross-field velocity is directed inwards in those regions where $\nabla_\perp \ln(n_0/B^2) < 0$ and outwards when the gradient changes sign, while the flux contribution due to the $n_0 \langle u_{\perp e1} h_{e1}^* \rangle$ term presents the opposite behavior.

Substituting the expressions for $\langle u_{\perp e1} h_{e1}^* \rangle$ and $u_{\perp e2}$ in Eq. (25) and discarding any $O(\varepsilon)$ term,

$$(n_e u_{\perp e})_2 = n_0 c_e k^2 \rho_e^3 \omega_{LH}^2 \frac{k_\theta \omega_{ri} \gamma}{\left(\omega_{ri}^2 + \gamma^2\right)^2} \frac{e^2 |\phi_1|^2}{T_e^2}\,. \tag{26}$$

Equation (26) shows that the second order electron flux has the same sign of the second order velocity $\langle u_{\perp e1} h_{e1}^* \rangle$. Thus, the cross-field electron current is directed against the perpendicular gradient of n_0/B^2. Instabilities then act to attenuate gradient-driven drifts present at the equilibrium.

Copyright 2025 by the Electric Rocket Propulsion Society. All rights reserved.

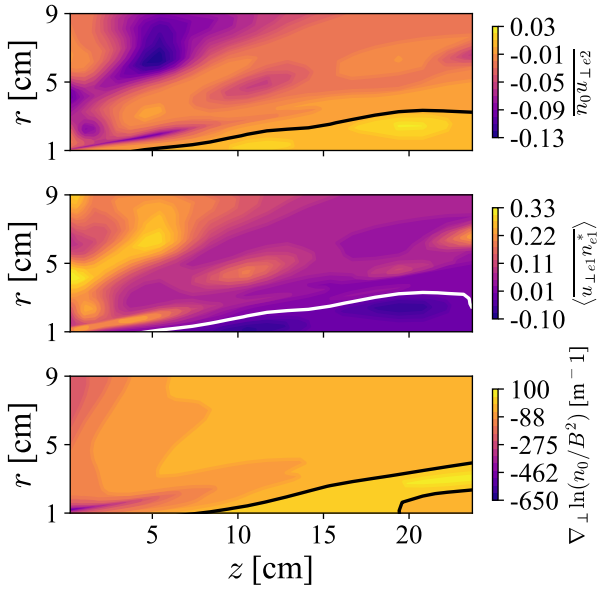

Figure 4: Comparison between the direction of the two components of the second-order cross-field electron flux and the direction of the gradient $\nabla_\perp \ln(n_0/B^2)$. The second-order fluxes have been normalized with the electron thermal flux $n_0 c_e$ and the wave amplitude $e^2|\phi_1|^2/T_e^2$. The black/white lines correspond where the plotted values pass through 0.

5 Preliminary description of a mixed PIC/PIF model for $E \times B$ discharges

PICASO [44, 29, 45, 46, 47, 48] (Particle-In-Cell Advanced SimulatOr) is an electrostatic 2D Particle-In-Cell code developed to simulate plasma flows in low-collisionality plasmas. PICASO is a 2D3V, explicit, momentum-preserving PIC code that makes use of standard algorithms for the movement and weighing of the electron and ion macro-particles in a uniform, rectangular mesh. It uses the Boris leapfrog algorithm [49] to advance particles in two spatial and three velocity space dimensions, particles are weighted on the cell nodes through a bilinear interpolating function to reconstruct the species' macro-properties at the mesh nodes, and electromagnetic fields are linearly interpolated on each particle position. The electric potential values at all domain nodes are obtained through the solution of Poisson's equation

$$\varepsilon_0 \nabla^2 \phi = e(n_e - n_i) \tag{27}$$

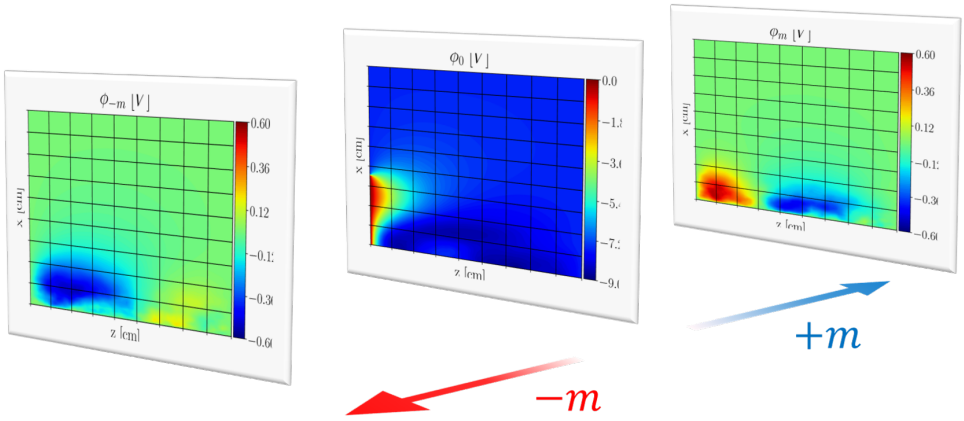

Figure 5: Schematization of a multi-formulation code with 2D Particle-in-Cell scheme in the *r*-*z* direction and spectrally decomposed in the aziumthal direction.

Copyright 2025 by the Electric Rocket Propulsion Society. All rights reserved.

by means of its spatial discretization through second order finite difference schemes, and the resolution of the linear system thus obtained with Intel's MKL Pardiso solver[50]. Here ε_0 is the electric permittivity, ϕ the electrostatic potential and n_j the number density for the j-th species (i = ions, e = electrons). It has been mostly applied to simulate $E \times B$ discharges in the axial-radial ($z-r$) and axial-azimuthal ($z-\theta$) planes, in particular Hall Thruster plasmas. Its limitation to 2D geometries requires the use of semi-empirical models to add anomalous transport due to wall-particle interactions (in $z-\theta$ geometries) or due to azimuthal instabilities (in $z-r$ geometries), introduced by means of an *ad hoc* scattering to increase the effective collisionality of the plasma and to enhance particle cross-field motion.

The inclusion of the third direction (i.e., the azimuthal θ direction) is necessary to self-consistently capture the instability-driven transport. In a cylindrical plasma, the macroscopic fields can be naturally expressed as a Fourier series in θ taking advantage of the periodicity of the azimuthal direction. For example, the number density of the j species is

$$n_j(r,z,\theta) = n_{j_0}(r,z) + \sum_{m=1}^{N_m} \left(n_{j_m}^{+}(r,z)\cos(m\theta) + n_{j_m}^{-}(r,z)\sin(m\theta) \right) \tag{28}$$

with the azimuthally-averaged component being

$$n_{j_0} = \frac{1}{2\pi}\int_0^{2\pi} n_j(r,z,\theta)d\theta \ , \tag{29}$$

and with the m-th coefficients being

$$n_{j_m}^{+} = \frac{1}{\pi}\int_0^{2\pi} n_j(r,z,\theta)\cos(m\theta)d\theta \ , \qquad n_{j_m}^{-} = \frac{1}{\pi}\int_0^{2\pi} n_j(r,z,\theta)\sin(m\theta)d\theta \ . \tag{30}$$

This applies to the electric potential and field, as well. The value N_m corresponds to the maximum number of modes considered. With this addition, we are able to treat the full Vlasov's equation (here expressed in its formulation for cylindrical set of coordinates) for each species $p = i, e$,

$$\begin{aligned} &\frac{\partial f}{\partial t} + v_r\frac{\partial f}{\partial r} + \frac{v_\theta}{r}\frac{\partial f}{\partial \theta} + v_z\frac{\partial f}{\partial z} + \left(\frac{q_p E_r}{m_p} + \frac{q_p}{m_p}(\boldsymbol{v}\times\boldsymbol{B})_r + \frac{v_\theta^2}{r} \right)\frac{\partial f}{\partial v_r} \\ &\quad + \left(\frac{q_p E_\theta}{m_p} + \frac{q_p}{m_p}(\boldsymbol{v}\times\boldsymbol{B})_\theta - \frac{v_r v_\theta}{r} \right)\frac{\partial f}{\partial v_\theta} + \left(\frac{q_p E_z}{m_p} + \frac{q_p}{m_p}(\boldsymbol{v}\times\boldsymbol{B})_z \right)\frac{\partial f}{\partial v_z} = 0 \ ; \end{aligned} \tag{31}$$

from here, by averaging with respect to the azimuthal direction, multiplying each side of Eq. (31) by $-ev_\theta$ and integrating it in the velocity space, we get the azimuthally-averaged cross-field electron current

$$j_{e0r} = (\nabla\cdot\overline{\overline{p}}_{e0})_\theta + \frac{e^2}{2rB_z}\sum_{m=1}^{N_m}\left[m(\phi_m^{+}n_{em}^{-} - \phi_m^{-}n_{em}^{+}) \right] . \tag{32}$$

The r-z formulation of PICASO, being a 2D code, only retains the first term on the right-hand side, corresponding to the gyroviscous contribution. Its spectral extension to 3D allows for the addition for the second term, which represents the fluctuation-driven anomalous transport.

Figure 5 shows a schematic representation of the code's finite differencing (FD)/spectral architecture. Each of the density modes are first computed at the nodes of the 2D r-z physical grid. Then, making use of the linearity of Poisson's equation, each m-th density mode contributes uniquely to determine the m-th electric potential mode on each point of the grid. Then, the resulting electric field is reconstructed and applied at each particle's position. Note that, while the field's value has to be interpolated in the r-z plane at each particle's position, in the azimuthal direction no interpolation is needed as the field is a known function at any θ. This means that the field conserves spectral fidelity [34] at the particle's position, avoiding numerical phase mismatches and subsequent spurious instabilities.

A raw application of the spectral method would come from the increase of computational time required by the computation of each particle's contribution the the m-th density mode, scaling as $O(N_p N_m)$ [51]. A computationally-efficient spectral formulation would have to rely on Fast Fourier Transform (FFT) algorithms [52, 53], possibly reducing the computational times up to $O(N_p + N_m\log(N_m))$.

Copyright 2025 by the Electric Rocket Propulsion Society. All rights reserved.

5.1 Particle Weighting

Particle weighting remains unchanged in the (r,z) plane, while weighting in the θ is quite simple (as the shape of the density is already known). Weighting in PIC codes is just a simple counting of particles inside a predetermined spatial region, accounting for the distance from the geometric center of said region:

$$n_k(\boldsymbol{x}) = \sum_p w_p W(\boldsymbol{x} - \boldsymbol{x}_p) \tag{33}$$

with W a particular normalized weighting function, w_p the particle weight and $\boldsymbol{x}_p = r_p \mathbf{1}_r + z_p \mathbf{1}_z$ the particle position. In PICASO, the weighting of choice is bilinear, so that at the point (z_i, r_j)

$$n_k(z_i, r_j) = \frac{1}{V(z_i, r_j)} \sum_p w_p w_z(z_i - z_p) w_r(r_j - r_p) \tag{34}$$

with $V(r_i, z_j)$ is the control volume around the ij-th node. When considering the azimuthal direction, since the shape of each mode is known:

$$n_{km}^{+}(z_i, r_j) = \frac{1}{V(z_i, r_j)} \int_{2\pi} d\theta \sum_p w_z(z_i - z_p) w_r(r_j - r_p) S(\theta - \theta_p) \cos(m\theta), \tag{35}$$

with S a suitable particle shape function in θ, and similarly for n_{km}^{-}. Selecting for S the Dirac delta function δ, the integral yields the simple form

$$n_{km}^{+}(z_i, r_j) = \frac{1}{V(z_i, r_j)} \sum_p w_z(z_i - z_p) w_r(r_j - r_p) \cos(m\theta_p). \tag{36}$$

The handiness of δ in solving the integral comes at the cost of being a very difficult function to be reconstructed by a Fourier. This point is discussed in subsection 5.3.

5.2 Poisson's Equation and particle mover

Making use of this expansion, Poisson's equation can be written as

$$\nabla^2 \left(\phi_0(r,z) + \sum_{m=1}^{\infty} \left(\phi_m^{+}(r,z) \cos(m\theta) + \phi_m^{-}(r,z) \sin(m\theta) \right) \right) =$$
$$\frac{e}{\varepsilon_0} \left([n_{e0} - n_{i0}](r,z) + \sum_{m=1}^{\infty} \left(\left[n_{em}^{+} - n_{im}^{+} \right](r,z) \cos(m\theta) + \left[n_{em}^{-} - n_{im}^{-} \right](r,z) \sin(m\theta) \right) \right) . \tag{37}$$

As commented before, for virtue of orthogonality, Poisson's equation can be solved independently for each mode, i.e.

$$\left(\frac{\partial^2}{\partial z^2} + \frac{\partial^2}{\partial r^2} + \frac{1}{r}\frac{\partial}{\partial r} - \frac{m^2}{r^2} \right) \phi_m^{\pm}(r,z) = \frac{e}{\varepsilon_0} \left[n_{em}^{\pm} - n_{im}^{\pm} \right](r,z) . \tag{38}$$

The electric field is reconstructed from its modal components, interpolated at the (r_p, z_p) particle position on the physical grid, and exactly computed at the particle azimuthal coordinate θ_p,

$$\boldsymbol{E}(\boldsymbol{x}_p) = \sum_{m=0}^{\infty} \Bigg\{ - \left(\mathbf{1}_x \frac{\partial}{\partial x} + \mathbf{1}_z \frac{\partial}{\partial z} \right) \times$$
$$\left[\phi_m^{+}(r_p, z_p) \int S(\theta - \theta_p) \cos(m\theta) d\theta + \phi_m^{-}(r_p, z_p) \int S(\theta - \theta_p) \sin(m\theta) d\theta \right] +$$
$$\mathbf{1}_\theta \frac{m}{r_p} \left[\phi_m^{+}(r_p, z_p) \int S(\theta - \theta_p) \sin(m\theta) d\theta - \phi_m^{-}(r_p, z_p) \int S(\theta - \theta_p) \cos(m\theta) d\theta \right] \Bigg\} , \tag{39}$$

Copyright 2025 by the Electric Rocket Propulsion Society. All rights reserved.

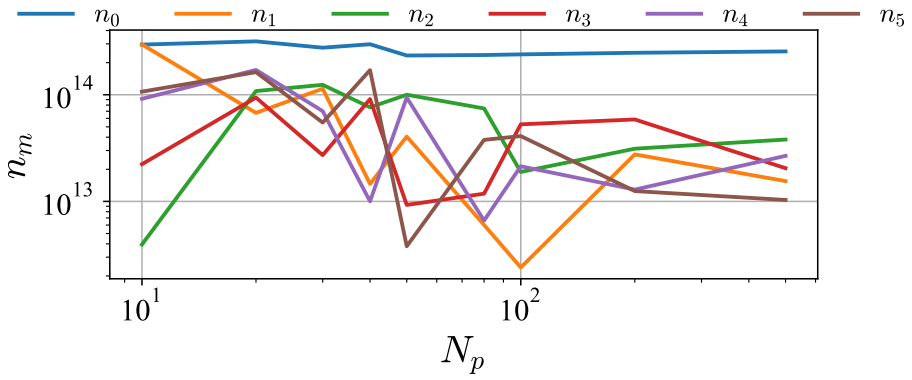

Figure 6: Comparisons of the values of n_0 and various n_ms, $m = 1$ to 4, as a function of N_p.

and then applied to the particle through Newton's 2nd law,

$$\dot{r}_p = v_{p_r} \tag{40}$$

$$r_p \dot{\theta}_p = v_{p\theta} \tag{41}$$

$$\dot{v_{p_r}} = \frac{q_p E_r}{m_p} + \frac{q_p}{m_p}(\boldsymbol{v}_p \times \boldsymbol{B})_r + \frac{v_\theta^2}{r} \tag{42}$$

$$\dot{v_{p\theta}} = \frac{q_p E_\theta}{m_p} + \frac{q_p}{m_p}(\boldsymbol{v}_p \times \boldsymbol{B})_\theta - \frac{v_r v_\theta}{r} \,. \tag{43}$$

The particles are then advanced in time through Boris' algorithm.

5.3 Particle distribution and shape along theta

A random arrangement of particles in the azimuthal direction can lead to the spurious appearance of important $m \neq 0$ even in axisymmetric configurations. This is due to the poor scaling between homogenity of the distribution and number of particles needed with Dirac delta as a shape function, as exemplified in Figure 6. Here, the various n_ms have been computed at varying number of particles contained in a cell in the r-z plane and distributed randomly in θ. The azimuthal modes n_m scale approximately as

$$\log n_m = \frac{1}{\sqrt{N_p}} \tag{44}$$

A somewhat axisymmetric distribution, with n_0 bigger than the other modes by at least an order of magnitude, is achieved at $N_p > 10^2$. Alternatively, the axisymmetry of the particles can be obtained by forcibly distributing them in an axisymmetric configurations, for example placing particles on circular ring, thus forcing $N_p = N_r N_{ppr}$ to be a multiple of the number of rings N_r, with N_{ppr} the number of particles per each ring. The resulting axisymmetry is shown in Figure 7: this solution can result useful in situations where the number of particles is too low to reach a satisfying distinction in the order of magnitudes between n_0 and the n_ms, for example at the injection plane in a MN.

Lastly, a discussion is needed for the particle shape function and its inherent relation with the maximum number of modes N_m. As stated beforehand, the Delta Dirac function $\delta(\theta)$ comes very handy when solving integrals in θ, but requires a high number of modes to be decently described by a Fourier series, its truncated Fourier representation δ_{N_m} being

$$\delta_{N_m}(\theta) = \frac{1}{\pi}\left(\frac{1}{2} + \sum_{m=1}^{N_m} \cos(m\theta)\right). \tag{45}$$

Copyright 2025 by the Electric Rocket Propulsion Society. All rights reserved.

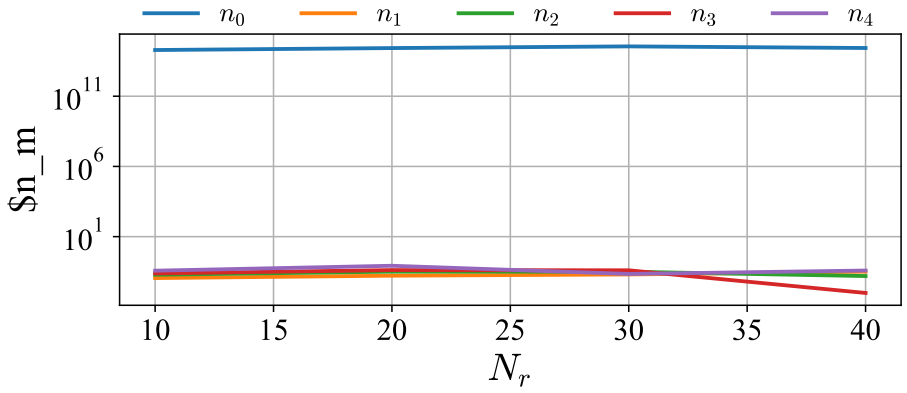

Figure 7: Same as Figure 6, but with the particles following an equi-spaced distribution on rings. The distinction of orders of magnitude between n_0 and the various n_ms does not change with the number of rings.

For a not-too-inaccurate representation of δ, a high number of modes is needed. Smoother shape functions, on the other hand, may require less modes to be accurately replicated. Their choice could be entirely arbitrary and out of commodity of integration (i.e., choosing a Gaussian), or physically sound (i.e., using Green's function of Poisson's equation). These last aspects, together with the existence of an optimal choice for the shape function, are still being investigated.

6 Summary and future works

In this work, the derivation of the dispersion relation relevant for electrostatic fluid waves in a 2D-inhomogenous $E \times B$ discharge in the low-to-mid frequency regime, with subthermal drifts and 3D propagation, has been presented. Its main unstable modes have been discussed, and compared against known results from literature. In particular, a generalization of the MTSI has been obtained, with the novel inclusion of gradients of the zeroth-order plasma quantities parallel to $\boldsymbol{B}$, extending it to drifts of the order $|\Delta| < \omega_{LH}$. Moreover, a modification of the classical LHDI has been obtained, finding that parallel effects can lead to an extension of the parametric region of instability for certain combinations of the perpendicular gradients of B and ϕ.

This dispersion relation has then been applied to PIC/fluid/wave simulation data obtained from Ref. [37], revealing that the model suggests the most unstable modes to be mainly directed in the azimuthal direction, and in the frequency range 100 kHz - 1 MHz, in qualitative agreement with the available experimental data.

Lastly, a quasi-linear model has been developed and applied to the same simulation data, indicating a second-order cross-field electron flux directed against the zeroth-order gradient of n_0/B^2. Quasi-linear diffusion is then found to act againnst the very same gradients that cause inter-species drifts in the first place, giving rise to instabilities. In a MN nozzle case, this would mean that unstable phenomena would drive the plasma away from the axis.

This first part of the work has been published in [39].

As a final step, the preliminary mathematical modeling of a mixed PIC/PIF code for the study of instability-driven transport in $E \times B$ discharges has been presented. The main advantages of using a spectral framework, such as spectral fidelity and energy conservation, as well as its computational challenges have been highlighted, and the need of suitable shape functions has been discussed. The development of such a code would help the study of complex time-varying physics and mode mixing in practical MN configurations, where the 2D topology of the magnetic field requires the description of plasma dynamics in the three dimensions.

Copyright 2025 by the Electric Rocket Propulsion Society. All rights reserved.

This last part of the research represents a work-in-progress, and the next efforts will be directed towards trustworthy simulations of simple 3D plasma configurations, such as plasma columns, and the comparison of eventual time-varying phenomena with the linear theory previously discussed. Once this is accomplished, simulations of non-linear transport in MNs will represent the natural next step of this work.

Acknowledgments

This project has received funding from the European Research Council (ERC) under the European Union's Horizon 2020 research and innovation programme (Starting Grant project ZARATHUSTRA, grant agreement No 950466).

The participation of E. Ahedo lies within the R&D project PID2022-140035OB-I00 (HEEP) funded by MCIN/AEI/10.13039/501100011033 and by "ERDF A way of making Europe".

Data availability

The simulation dataset used in this work can be accessed freely on `https://doi.org/10.5281/zenodo.10641401` under the license terms detailed therein.

The `SymPy` notebook used as computational support for the derivations in the Appendix can be freely accessed on `https://doi.org/10.5281/zenodo.16783071` under the license terms detailed therein.

References

[1] H. Kaufman, "Technology of closed-drift thrusters," *AIAA Journal*, vol. 23, pp. 78–87, 1985.

[2] D. Goebel, I. Katz, and I. Mikellides, *Fundamentals of electric propulsion*. John Wiley & Sons, 2023.

[3] E. Ahedo, "Plasmas for space propulsion," *Plasma Physics and Controlled Fusion*, vol. 53, no. 12, p. 124037, 2011.

[4] C. Charles, R. Boswell, and M. Lieberman, "Xenon ion beam characterization in a helicon double layer thruster," *Applied Physics Letters*, vol. 89, no. 26, p. 261503, 2006.

[5] J. Navarro-Cavallé, M. Wijnen, P. Fajardo, and E. Ahedo, "Experimental characterization of a 1 kW helicon plasma thruster," *Vacuum*, vol. 149, pp. 69–73, 2018.

[6] K. Takahashi, "Helicon–type radiofrequency plasma thrusters and magnetic plasma nozzles," *Reviews of Modern Plasma Physics*, vol. 3, p. 3, 2019.

[7] H. Kosmahl, D. Miller, and G. Bethke, "Plasma acceleration with microwaves near cyclotron resonance," *Journal of Applied Physics*, vol. 38, no. 12, pp. 4576–4582, 1967.

[8] J. Sercel, "Electron-cyclotron-resonance (ECR) plasma thruster research," in *24th Joint Propulsion Conference*, no. 2916, 1988.

[9] M. R. Inchingolo, M. Merino, and J. Navarro-Cavallé, "Plume characterization of a waveguide ecr thruster," *Journal of Applied Physics*, vol. 133, no. 11, p. 113304, 2023.

[10] V. Désangles, D. Packan, J. Jarrige, S. Peterschmitt, P. Dietz, S. Scharmann, K. Holste, and P. J. Klar, "ECRA thruster advances: 30w and 200w prototypes latest performances," *Journal of Electric Propulsion*, vol. 2, no. 1, p. 10, 2023.

[11] S. Andersen, V. Jensen, P. Nielsen, and N. D'Angelo, "Continuous supersonic plasma wind tunnel," *Phys. Fluids*, vol. 12, no. 3, pp. 557–560, 1969.

Copyright 2025 by the Electric Rocket Propulsion Society. All rights reserved.

[12] R. Gerwin, G. Marklin, A. Sgro, and A. Glasser, "Characterization of plasma flow through magnetic nozzles," Tech. Rep. AFSOR AL-TR-89-092, Los Alamos National Laboratory, 1990.

[13] M. Merino and E. Ahedo, "Magnetic nozzles for space plasma thrusters," in *Encyclopedia of Plasma Technology* (J. L. Shohet, ed.), vol. 2, pp. 1329–1351, Taylor and Francis, 2016.

[14] I. D. Kaganovich, A. Smolyakov, Y. Raitses, E. Ahedo, I. G. Mikellides, B. Jorns, F. Taccogna, R. Gueroult, S. Tsikata, A. Bourdon, J.-P. Boeuf, M. Keidar, A. T. Powis, M. Merino, M. Cappelli, K. Hara, J. A. Carlsson, N. J. Fisch, P. Chabert, I. Schweigert, T. Lafleur, K. Matyash, A. V. Khrabrov, R. W. Boswell, and A. Fruchtman, "Perspectives on physics of E×B discharges relevant to plasma propulsion and similar technologies," *Physics of Plasmas*, vol. 27, no. 12, pp. 120–601, 2020.

[15] K. Takahashi, C. Charles, and R. W. Boswell, "Wave-driven electron inward transport in a magnetic nozzle," *Scientific Reports*, vol. 12, no. 1, p. 20137, 2022.

[16] D. Maddaloni, F. Boni, V. Désangles, B. Bayón-Buján, M. Merino, and F. Terragni, "Experimental characterization of oscillations in the magnetic nozzle of an electron cyclotron resonance thruster," in 38th *International Electric Propulsion Conference*, no. IEPC-2024-387, (Toulouse, France, June 23-28), Electric Rocket Propulsion Society, 2024.

[17] D. Maddaloni, B. Bayón-Buján, J. Navarro-Cavallé, and M. Merino, "Low-frequency oscillations in the magnetic nozzle of a helicon plasma thruster," *Plasma Sources Scinece and Technology*, vol. 34, no. 4, p. 045008, 2025.

[18] S. Hepner, B. Wachs, and B. Jorns, "Wave-driven non-classical electron transport in a low temperature magnetically expanding plasma," *Applied Physics Letters*, vol. 116, no. 26, p. 263502, 2020.

[19] A. E. Vinci, *Physics of magnetic nozzles and helicon plasma discharges*. PhD thesis, Université d'Orléans, 2022.

[20] N. A. Krall and P. C. Liewer, "Low-frequency instabilities in magnetic pulses," *Physical Review A*, vol. 4, no. 5, pp. 2094–2103, 1971.

[21] R. Davidson and N. Gladd, "Anomalous transport properties associated with the lower-hybrid-drift instability," *The Physics of Fluids*, vol. 18, no. 10, pp. 1327–1335, 1975.

[22] J. D. Huba and C. S. Wu, "Effects of a magnetic field gradient on the lower hydrid drift instability," *Physics of Fluids*, vol. 19, no. 7, pp. 988–994, 1976.

[23] Y. Sakawa, C. Joshi, P. Kaw, F. Chen, and V. Jain, "Excitation of the modified Simon–Hoh instability in an electron beam produced plasma," *Physics of Fluids B: Plasma Physics*, vol. 5, no. 6, pp. 1681–1694, 1993.

[24] A. Simon, "Instability of a partially ionized plasma in crossed electric and magnetic fields," *The Physics of Fluids*, vol. 6, no. 3, pp. 382–388, 1963.

[25] O. Buneman, "Instability of electrons drifting through ions across a magnetic field," *Journal of Nuclear Energy. Part C, Plasma Physics, Accelerators, Thermonuclear Research*, vol. 4, no. 2, pp. 111–117, 1962.

[26] E. Ott, J. B. McBride, J. H. Orens, and J. P. Boris, "Turbulent heating in computer simulations of the modified plasma two-stream instability," *Phys. Rev. Lett.*, vol. 28, pp. 88–91, Jan 1972.

[27] N. Gladd, "The lower hybrid drift instability and the modified two stream instability in high density theta pinch environments," *Plasma Physics*, vol. 18, no. 1, p. 27, 1976.

Copyright 2025 by the Electric Rocket Propulsion Society. All rights reserved.

[28] F. Petronio, A. Tavant, T. Charoy, A. Alvarez Laguna, A. Bourdon, and P. Chabert, "Conditions of appearance and dynamics of the modified two-stream instability in E× B discharges," *Physics of Plasmas*, vol. 28, no. 4, 2021.

[29] A. Marín-Cebrián, E. Bello-Benítez, A. Domínguez-Vázquez, and E. Ahedo, "Non-maxwellian electron effects on the macroscopic response of a hall thruster discharge from an axial–radial kinetic model," *Plasma Sources Science and Technology*, vol. 33, p. 025008, 2 2024.

[30] L. Garrigues, I. Boyd, and J. Boeuf, "Computation of Hall thruster performance," *Journal of Propulsion and Power*, vol. 17, no. 4, pp. 772–779, 2001.

[31] S. Di Fede, M. Manente, P. J. Comunian, and M. Magarotto, "Magnetic nozzle performance in a cluster of helicon plasma thrusters," *Plasma Sources Science and Technology*, vol. 32, no. 6, p. 065013, 2023.

[32] M. Guaita, E. Ahedo, and M. Merino, "Pic/fluid simulations of the plasma expansion in a planar magnetic arch," *Plasma Sources Science and Technology*, vol. 34, p. 015007, jan 2025.

[33] E. Bello-Benítez, A. Marín-Cebrián, and E. Ahedo, "Effect of injection conditions on the nonlinear behavior of the ECDI and related turbulent transport," *Physics of Plasmas*, vol. 32, no. 1, p. 012307, 2025.

[34] C.-K. Huang, Y. Zeng, Y. Wang, M. Meyers, S. Yi, and B. Albright, "Finite grid instability and spectral fidelity of the electrostatic particle-in-cell algorithm," *Computer Physics Communications*, vol. 207, pp. 123–135, 2016.

[35] F. Taccogna and L. Garrigues, "Latest progress in Hall thrusters plasma modelling," *Reviews of Modern Plasma Physics*, vol. 3, no. 1, p. 12, 2019.

[36] E. Evstatiev and B. Shadwick, "Variational formulation of particle algorithms for kinetic plasma simulations," *Journal of Computational Physics*, vol. 245, pp. 376–398, 2013.

[37] P. Jiménez, J. Zhou, J. Navarro-Cavallé, P. Fajardo, M. Merino, and E. Ahedo, "Analysis of a cusped helicon plasma thruster discharge," *Plasma Sources Science and Technology*, vol. 32, no. 10, p. 105013, 2023.

[38] M. Ripoli, M. Merino, and E. Ahedo, "Analysis of drift instabilities in magnetic nozzles," in 38th *International Electric Propulsion Conference*, no. IEPC-2024-506, (Toulouse, France, June 23-28), Electric Rocket Propulsion Society, 2024.

[39] M. Ripoli, E. Ahedo, and M. Merino, "Drift-gradient instabilities in a plasma with 2D gradient effects: Application to a magnetic nozzle," *Physics of Plasmas*, vol. 32, p. 092113, 09 2025.

[40] E. Bello-Benítez and E. Ahedo, "Axial-azimuthal, high-frequency modes from global linear-stability model of a Hall thruster," *Plasma Sources Science and Technology*, vol. 30, no. 3, p. 035003, 2021.

[41] J. Ramos, "General expression of the gyroviscous force," *Physics of Plasmas*, vol. 12, no. 11, p. 112301, 2005.

[42] J. J. Ramos, E. Bello-Benítez, and E. Ahedo, "Local analysis of electrostatic modes in a two-fluid E x B plasma," *Physics of Plasmas*, vol. 28, no. 5, p. 052115, 2021.

[43] J. McBride, E. Ott, J. Boris, and J. Orens, "Theory and simulation of turbulent heating by the modified two-stream instability," *The Physics of Fluids*, vol. 15, no. 12, pp. 2367–2383, 1972.

[44] A. Marín-Cebrián, E. Bello-Benítez, A. Domínguez-Vázquez, and E. Ahedo, "Macroscopic response of a Hall thruster discharge from an axial-radial PIC model," in 76th *Gaseous Electronics Conference*, (Ann Arbor, MI, October 9-13), 2023.

Copyright 2025 by the Electric Rocket Propulsion Society. All rights reserved.

[45] A. Marín-Cebrián, E. Bello-Benítez, E. Ahedo, and A. Domínguez-Vázquez, "Kinetic electron effects in a Hall thruster discharge with a curved magnetic field topology," in 38th *International Electric Propulsion Conference*, no. IEPC-2024-387, (Toulouse, France, June 23-28), Electric Rocket Propulsion Society, 2024.

[46] E. Bello-Benítez, A. Marín-Cebrián, J. J. Ramos, and E. Ahedo, "Two-dimensional kinetic simulation of electrostatic instabilities in a Hall plasma," in 37th *International Electric Propulsion Conference*, no. IEPC-2022-314, (Boston, MA, June 19-23), Electric Rocket Propulsion Society, 2022.

[47] E. Bello-Benítez, A. Marín-Cebrián, and E. Ahedo, "Effect of injection conditions on the nonlinear behavior of the ECDI and related turbulent transport," 2024. Pre-print available at https://arxiv.org/pdf/2405.08761.

[48] E. Bello-Benítez, *Analysis of turbulent transport in Hall-effect plasma thrusters*. PhD thesis, Universidad Carlos III de Madrid, Leganés, Spain, 2024.

[49] R. Hockney and J. Eastwood, *Computer simulation using particles*. CRC Press, Boca Ratón, FL, 1988.

[50] "Mkl." `https://www.intel.com/content/www/us/en/developer/tools/oneapi/onemkl.html#gs.if6snh`.

[51] C. N. Shen, A. Cerfon, and S. Muralikrishnan, "A particle-in-fourier method with semi-discrete energy conservation for non-periodic boundary conditions," *Journal of Computational Physics*, vol. 519, p. 113390, 2024.

[52] P. Duhamel and M. Vetterli, "Fast fourier transforms: A tutorial review and a state of the art," *Signal Processing*, vol. 19, no. 4, pp. 259–299, 1990.

[53] V. S. Tutatchikov, "Two-dimensional fast fourier transform: Batterfly in analog of Cooley-Tukey algorithm," in *2016 11th International Forum on Strategic Technology (IFOST)*, pp. 495–498, 2016.

Copyright 2025 by the Electric Rocket Propulsion Society. All rights reserved.